Supplemental Material

Formation and stability of reduced TiO_x layers on anatase TiO_2(101): identification of a novel Ti_2O_3 phase

Xunhua Zhao∗, Sencer Selcuk, and Annabella Selloni∗

Department of Chemistry, Princeton University,

Princeton, NJ 08544, USA †

1. Computational Methods and Models

Spin polarized DFT calculations were carried out within the plane-wave pseudopotential scheme as implemented in the Quantum ESPRESSO package [1], using the generalized gradient approximation (GGA) of Perdew-Burke-Ernzerhof (PBE) [2] with on-site Coulomb repulsion U on Ti 3d orbitals [3]. As a default value, we used U = 3.0 eV, which has been reported to ensure a similar accuracy for both TiO_2 and Ti_2O_3 [4]. To study the relative stabilities of csp-Ti_2O_3 and α-Ti_2O_3, we performed calculations using 10 different U values in the range 0.0 – 5.0 eV, which encompasses the values most typically used for reduced TiO_2 [5], as well as the hybrid functional HSE06 by Heyd, Scuseria and Ernzerhof [6,7], which is generally reported to perform well for semiconducting oxides, including TiO_2 [8]. For HSE06 calculations, the implementation in the FHI-aims code [9] was employed, along with default "tight" settings. For PBE+U calculations, we used ultra-soft pseudopotentials [10] with cutoff energies of 35 and 280 Ry for the smooth part of the electronic wavefunctions and augmented charge density, respectively. For bulk calculations, we sampled the Brillouin-zone using 6×6×6 and 3×9×9 k-point grids for α-Ti_2O_3 and csp-Ti_2O_3, respectively, which were sufficiently dense to converge total energies to better than 1 meV/Ti atom. For surface calculations, Γ-point sampling was used, with vacuum distance between neighboring slabs larger than 11 Å. A 5-mRy Gaussian smearing was applied. For each functional and U value used, both the cell parameters and the internal ion coordinates were optimized with the Broyden-Fletcher-Goldfarb-Shanno (BFGS) algorithm (force threshold = 10^{-3}eV /Å, energy threshold 10^{-5} Ry).

Surface calculations were performed starting from an anatase (101) slab with 7 TiO_2 layers and a (1×3) surface supercell to construct reduced systems containing n contiguous CSPs (n=0,1,2,3,4,5,6) and 7-n TiO_2 layers; these slab models are denoted nCSP@(7-n)TiO_2 in the

following. Fig. 1 illustrates how the first CSP is generated; additional CPSs in deeper layers can be generated in similar way. Extensive searches of the preferred geometric, electronic and magnetic configurations were carried out in order to identify the ground state of each *n*CSP@(7-*n*)TiO_2 model. In all cases the best solution was obtained by fixing the total magnetization to zero. O-vacancy formation energies (E_{form}) were calculated as $E_{\text{form}} = E_{n\text{Vo}} - E_{\text{pristine}} + \frac{n}{2}E_{O_2}$, where *n* is the number of oxygen vacancies and the first two terms are the total energy of the slab with and without vacancies respectively, the last term is the total energy of an oxygen molecule.

Below we present a few tests of our computational setup.

1.1 ***Lattice Parameters***

The lattice constants of csp-Ti_2O_3, α-Ti_2O_3 and anatase TiO_2 calculated at the PBE, PBE+*U* (*U*=3.0) and HSE06 levels are reported in Table S1. For HSE06 and PBE, deviations of α-Ti_2O_3 and anatase TiO_2 lattice parameters from experiment are smaller than 1% and 2%, respectively, whereas PBE+*U* overestimates the α-Ti_2O_3 lattice constants by as much as 4.24%. Since no experimental data is available for csp-Ti_2O_3, HSE06 values are used as a reference. The parameters of csp-Ti_2O_3 optimized with PBE+*U* are relatively close to those given by HSE06, whereas deviations of PBE parameters from HSE06 are very large, in the range of 4.5-6.9%. This may be attributed to the different magnetic configurations predicted by the two methods.

TABLE S1: Optimized lattice constants (in Å) of csp-Ti_2O_3, α-Ti_2O_3 and anatase TiO_2, obtained from PBE, PBE+*U* (*U*=3.0 eV) and HSE06 calculations. Values in parentheses are percent deviations from experimental values [11] in the case of α-Ti_2O_3 and anatase TiO_2, while they are deviations from HSE06 values for csp-Ti_2O_3. Calculations used a variable cell optimization without symmetry constraints. For α-Ti_2O_3 this resulted in a small deviation from perfectly rhombohedral symmetry.

Latt.	**csp-Ti_2O_3**			**α-Ti_2O_3**			**anatase TiO_2**		
	PBE	PBE+*U*	HSE06	PBE	PBE+*U*	HSE06	PBE	PBE+*U*	HSE06
a	3.98(4.46)	3.90(2.36)	3.81(0.0)	5.52(1.75)	5.65(4.24)	5.42(0.03)	3.78(0.34)	3.83(1.22)	3.76(-0.69)
b	2.95(-6.94)	3.16(0.0)	3.17(0.0)	5.51(1.68)	5.58(2.90)	5.42(0.01)	3.78(0.34)	3.83(1.22)	3.76(-0.77)
c	9.05(-5.93)	9.56(0.62)	9.62(0.0)	5.52(1.75)	5.65(4.24)	5.42(0.00)	9.665(1.27)	9.70(1.65)	9.63(0.91)
c/a	2.27(-9.92)	2.45(2.78)	2.52(0.0)	1.00(0.00)	1.00(0.00)	1.00(0.00)	2.55(0.01)	2.53(0.00)	2.56(0.02)

1.2 ***Reaction energy for the reduction of TiO_2 to Ti_2O_3***

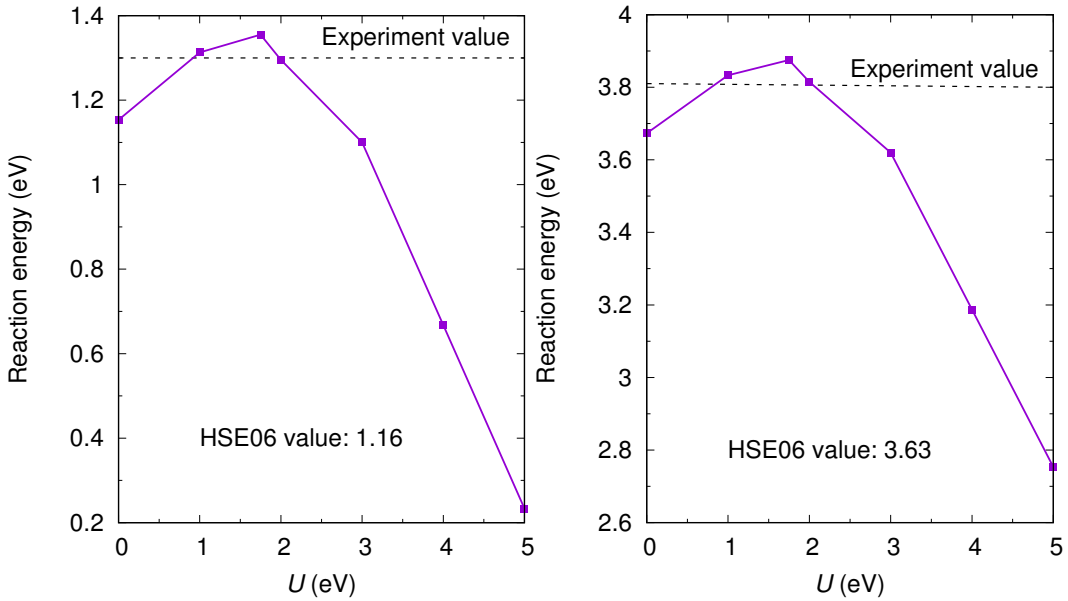

FIG. S1. Energy of the reactions $2TiO_2 + H_2 \rightarrow Ti_2O_3 + H_2O$ (left) and $2TiO_2 \rightarrow Ti_2O_3 + 1/2O_2$ (right) as a function of *U*. Rutile TiO_2 and α-Ti_2O_3 are used as in other studies and experiment [4,12].

TABLE S2: Energy (in eV) of the reduction reactions $2TiO_2 + H_2 \rightarrow Ti_2O_3 + H_2O$ and $2TiO_2 \rightarrow Ti_2O_3 + 1/2\ O_2$ obtained using PBE+*U* with various *U* values (in eV) and HSE06. Rutile TiO_2 and α-Ti_2O_3 are considered as in experiment.

Method	$2TiO_2 + H_2 \rightarrow Ti_2O_3 + H_2O$	$2TiO_2 \rightarrow Ti_2O_3 + 1/2O_2$
U=0	1.15	3.67
U=1	1.31	3.83
U=1.75	1.36	3.88
U=2	1.30	3.82
U=3	1.10	3.62
U=4	0.67	3.19
U=5	0.23	2.75
HSE06	1.16	3.63
Exp.	1.30	3.81

Figure S1 and Table S2 show the reaction energies of rutile Ti_2O_3 reduction. Our results agree well with previous studies [4,12] where PBE+*U* was also used. It appears that large *U* values, notably $U > 3$ eV, give reaction energies that deviate strongly from the experiment, while the best agreement with experiment is obtained with U values between 1 and 2 eV. It is known however that such small *U* values do not describe well the electronic structure of isolated oxygen vacancies [13]. A significantly better description is obtained with *U*=3.0 eV, which gives reaction energies that are underestimated only by ~ 0.2 eV, as found also with HSE06.

2 Role of configurational entropy in the relative stability of CSPs and well-separated VOs:

As shown in Table I (main text), DFT calculations predict that the CSP phase is energetically favored over isolated V_Os by *at least* 0.28 eV per V_O (at T = 0 K). However, the lower configurational entropy (S_{conf}) associated with ordering of the V_Os might destabilize the CSP phase at high T compared to disordered V_Os. We estimate S_{conf} for disordered V_Os using Boltzmann's entropy formula $S_{conf} = k_B \ln W$, where W is the number of possible configurations for the system at constant total energy. For the CSP phase, we take $S_{conf} = 0$, as it requires perfect ordering of V_Os.

V_Os in anatase have a slightly repulsive interaction (Table I of main text), but for simplicity we first assume that they do not interact, so that the total energy of the system does not depend on their separation. In this case, the number of possible configurations W of n_{vac} V_Os over N oxygen sites is simply:

$$W = \frac{N!}{(N - n_{vac})!\, n_{vac}!}$$

We first calculate S_{conf} for a slab with a 1 × 3 surface supercell (similar to the models used in the DFT calculations) and varying thickness. This slab has 12 V_O sites per (101) layer and requires at least 6 V_Os for CSP formation (in the following the minimum V_O concentration for CSP formation is denoted as VO_{min}). We plot our results in Figure S1a, where the solid and dashed blue curves show S_{conf} at V_O concentration $[V_O] = VO_{min}$ and $10 \cdot VO_{min}$, respectively. We can see that at the higher V_O concentration S_{conf} for the disordered V_O phase is smaller, so that CSP formation becomes more favorable, as expected. The right y-axis in the same figure shows the

minimum T required for disordered V_Os to overcome the stability of the CSP phase at a given S_{conf}. Apparently, even when $[V_O] = VO_{min}$, a very thick slab or a very high T is required to destabilize the CSP phase over disordered V_Os.

The assumption that the vacancies do not interact overestimates the number of possible configurations and provides an upper-limit for the actual S_{conf} of disordered V_Os; hence it underestimates the stability of CSPs. We can also obtain a lower limit for the actual S_{conf} by assuming each V_O at a particular site prohibits formation of new V_Os on the *k* nearest sites; we can count the number of prohibited configurations and then deduct this number from W. A formula that counts all the prohibited configurations at least once can be obtained as follows. To place the first V_O (among our n_{vac} vacancies) we can choose any one site from the *N* total sites, and for the next V_O we can choose from one of the *k* sites that are blocked by the first. We can then arbitrarily place the remaining $(n_{vac} - 2)$ V_Os on the remaining $(N - 2)$ sites. Hence, a lower limit for the number of configurations can be calculated as:

$$W' = W - \frac{N \cdot k}{2} \cdot \frac{(N-2)!}{(N-n_{vac})!\,(n_{vac}-2)!}$$

In Fig. S1a, we also show the lower-limit curves for S_{conf} using different *k* values. Apparently, the effect of V_O interaction is limited, and it is actually negligible in larger systems.

For a closer comparison to experiment, we next consider the effect of using a larger surface supercell. Fig S1b compares S_{conf} per V_O for the small surface cell with 12 O sites per layer, already shown in Fig. S1a, to the same quantity calculated considering a larger surface cell with 160 O sites per layer. Fig. S1b shows that the surface size is largely irrelevant for the configurational entropy S_{conf} per V_O, and it is essentially negligible at higher V_O concentration.

Finally we note that these results, obtained using a slab model, can be easily extended also to nanoparticles. In fact, V_O diffusion is highly anisotropic in anatase, and in particular diffusion

toward the bulk occurs along the [100] direction at the anatase (101) surface [10]. Hence, only a region of the bulk layers that has the same area as the (101) surface is accessible to the V_Os, and the number of possible V_O configurations for a nanoparticle exposing {101} facets should then be comparable to that for a slab model exposing a similar surface area.

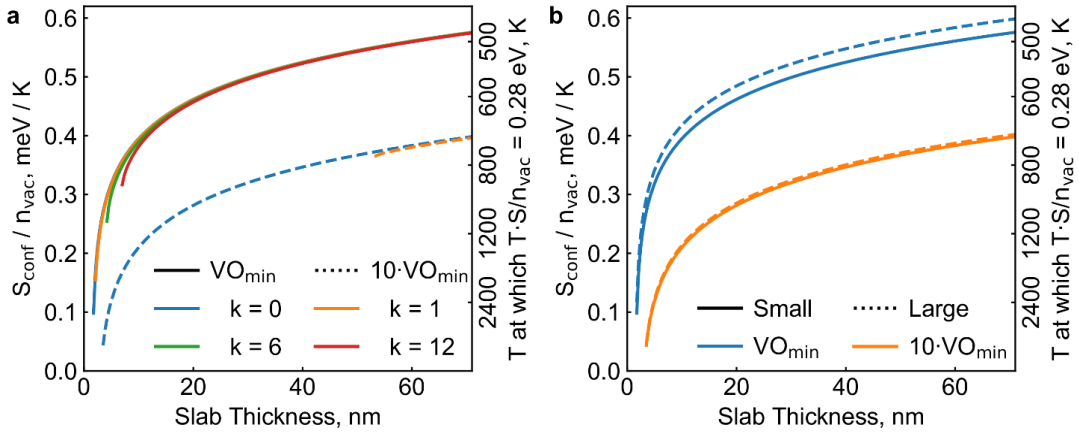

FIG. S2 Configurational entropy per V_O for disordered O-vacancies in an anatase (101) slab as a function of slab thickness. The right y-axis shows the minimum T required for disordered V_Os to overcome the stability of the CSP phase. (a) S_{conf} for a (1 × 3) anatase (101) slab. VO_{min} is the minimum V_O concentration required for CSP formation, and *k* is the number of neighboring sites of each V_O where formation of another V_O is blocked. Blue curves show the upper-limit of S_{conf} for different V_O concentrations, and the other curves show the lower-limits for different *k* values. (b) S_{conf} for the 1 × 3 "small" system in (a) is compared with a "large" system that has a surface cell with 160 VO sites per layer, and requires at least 80 V_Os for CSP formation.

3. Additional results for *n*CSP@TiO_2 slab models

3.1 Formation and surface/interface energies of CPS-TiO_2 structures

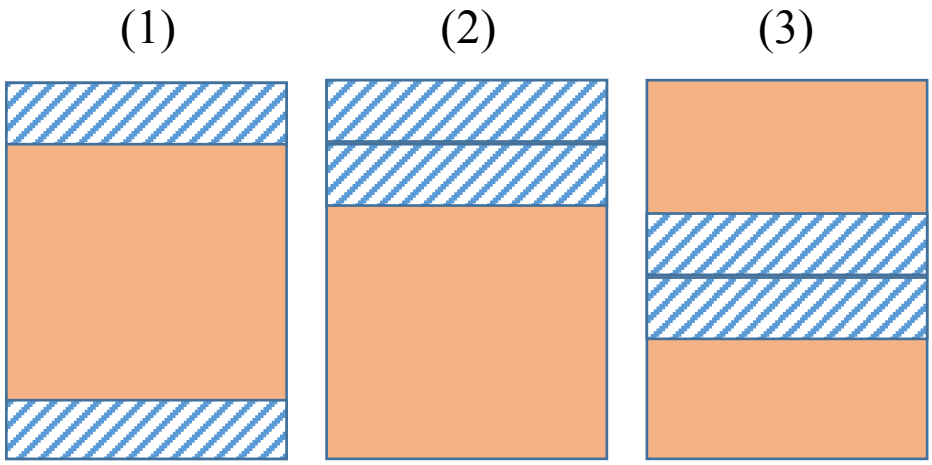

FIG. S3: Three forms of CSP distribution. Hatched and orange areas represent CSPs and regular TiO_2, respectively.

We first determined CSPs' formation energies for the model structures shown in Fig. S3 from the expression $E_{\mathrm{CSP}} = E_{\mathrm{total}} - nE_{\mathrm{TiO_2}} - mE_{\mathrm{Ti_2O_3}}$, where E_{total} is the total energy of the model, $E_{\mathrm{TiO_2}}$ and $E_{\mathrm{Ti_2O_3}}$ are the total energies per formula unit of bulk anatase TiO_2 and csp-Ti_2O_3, respectively, and n and m the corresponding numbers of units. We obtained $E_{\mathrm{CSP}} = 10.98$, 9.19, and 9.80 eV for Models (1), (2) and (3), respectively, in the case where each blue-shaded box in Fig. S3 corresponds to a single CSP, and $E_{\mathrm{CSP}} = 10.35$, 9.19, and 9.81 eV in the case where each blue-shaded box corresponds to two CSPs. These results clearly indicate that CSPs energetically prefer to aggregate and remain close to the surface (Model 2) rather than in the bulk.

The CSP's formation energies are then related to the formation of three different interfaces: Ti_2O_3-vacuum, TiO_2-vacuum and Ti_2O_3-TiO_2, with interface energies γ_a, γ_b and γ_c, respectively. Specifically, for the three cases shown in Figure S1 we write:

(1): $2(\gamma_a + \gamma_c) = E_{\mathrm{CSP}}^{(1)}/A$;

(2): $\gamma_a + \gamma_b + \gamma_c = E_{\mathrm{CSP}}^{(2)}/A$;

(3): $2(\gamma_b + \gamma_c) = E_{\mathrm{CSP}}^{(3)}/A$,

where A is the surface area. From these expressions we obtain: $\gamma_a = 0.57$ J/m^2, $\gamma_b = 0.54$ J/m^2 and $\gamma_c = 0.12$ J/m^2 for the Ti_2O_3-vacuum, TiO_2-vacuum and Ti_2O_3-TiO_2 interfaces, respectively. The value for the TiO_2-vacuum surface energy agrees well with the results of previous studies [14].

3.2 Electrostatic potential and work function

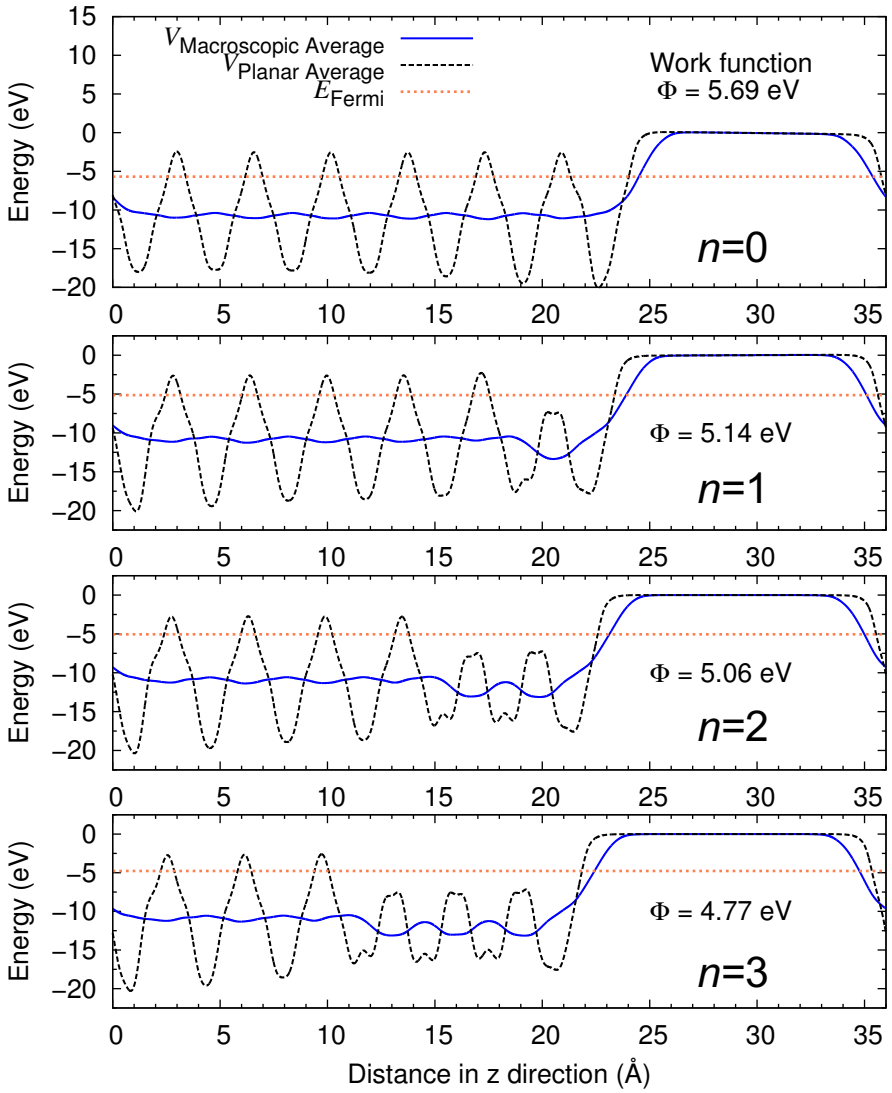

FIG. S4: Electrostatic potential profile along the surface normal for *n*CSP@(7-*n*)TiO_2 (*n*=0,1,2,3). The workfunction Φ for the different cases is indicated.

3.3 Layer-resolved density of states

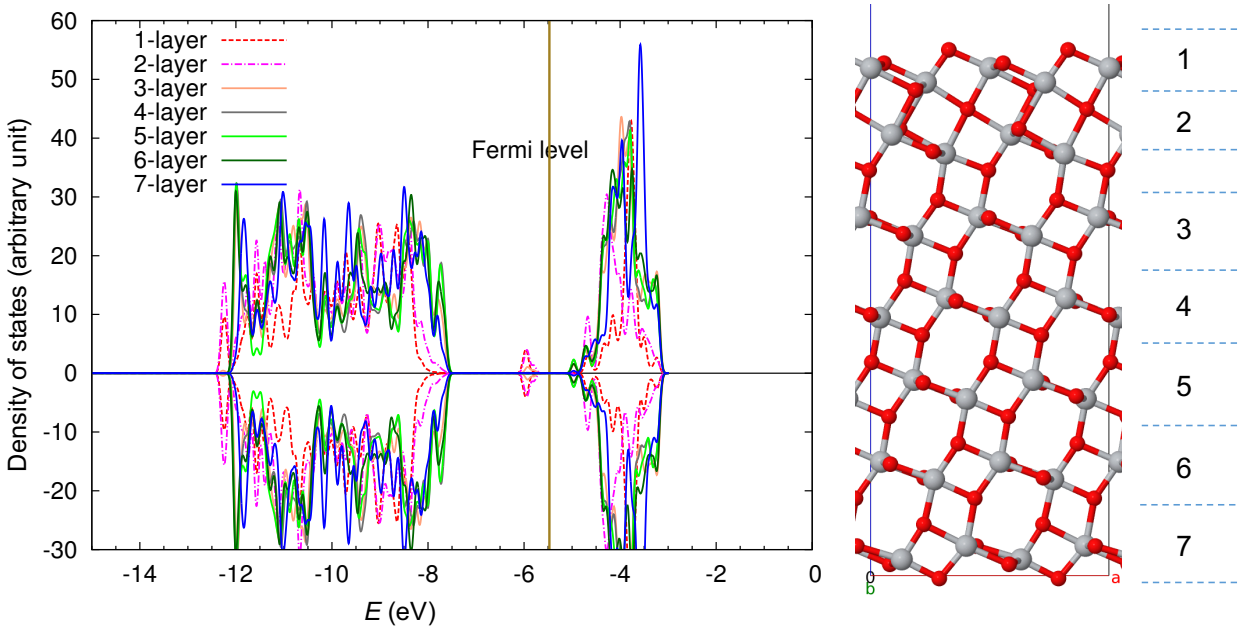

FIG. S5: Layer-resolved density of states (left) for 1CSP@6TiO_2 (right), computed using PBE+*U,* with *U*=3eV. Numbers on the far right define the different layers.

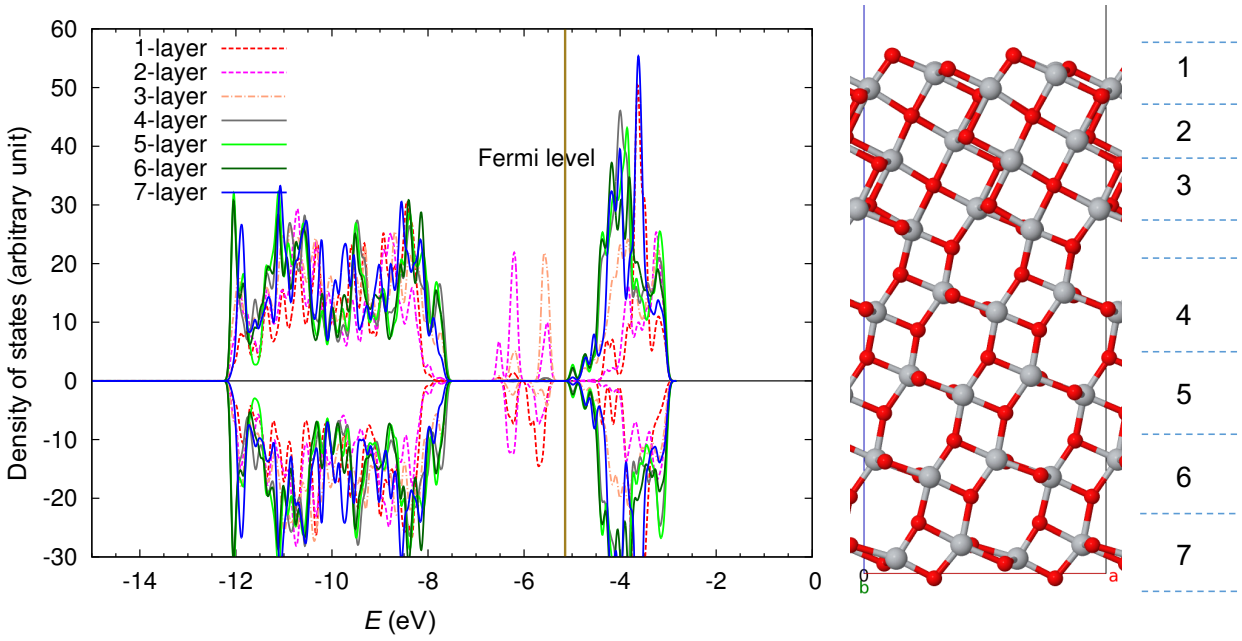

FIG. S6: Layer-resolved density of states (left) for 2CSP@6TiO_2 (right), computed using PBE+*U*, with *U*=3eV. Numbers on the far right define the different layers.

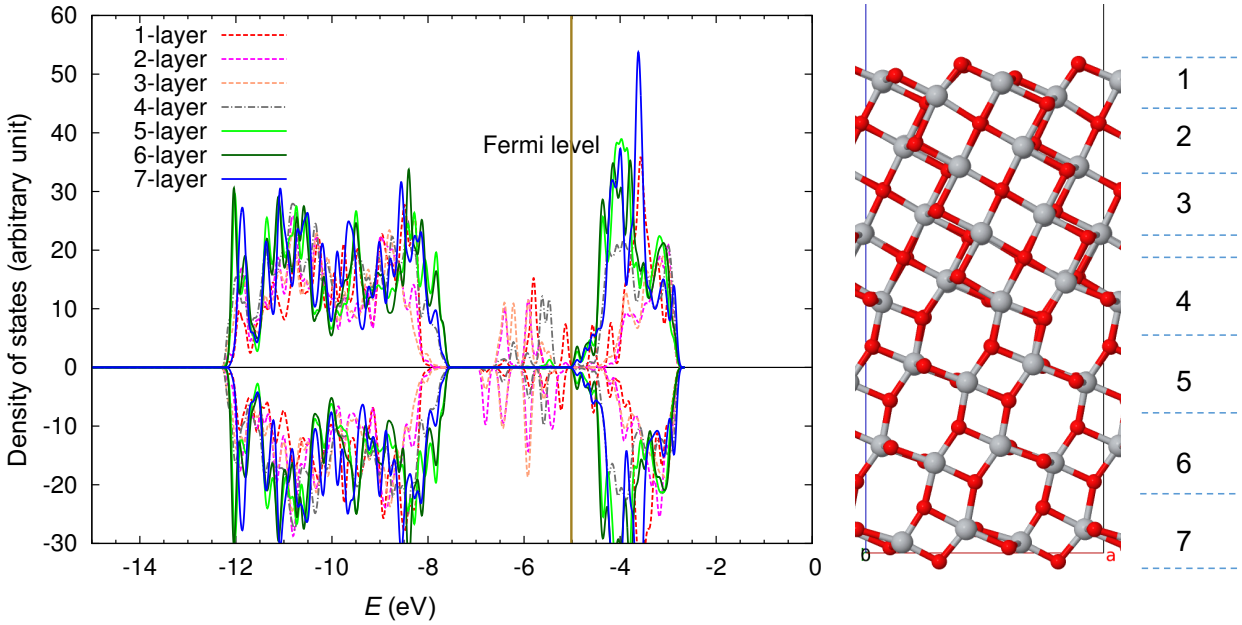

FIG. S7: Layer-resolved density of states (left) for 3CSP@6TiO_2 (right), computed using PBE+*U*, with *U*=3eV. Numbers on the far right define the different layers.

3.4 Stability in H_2/H_2O atmosphere

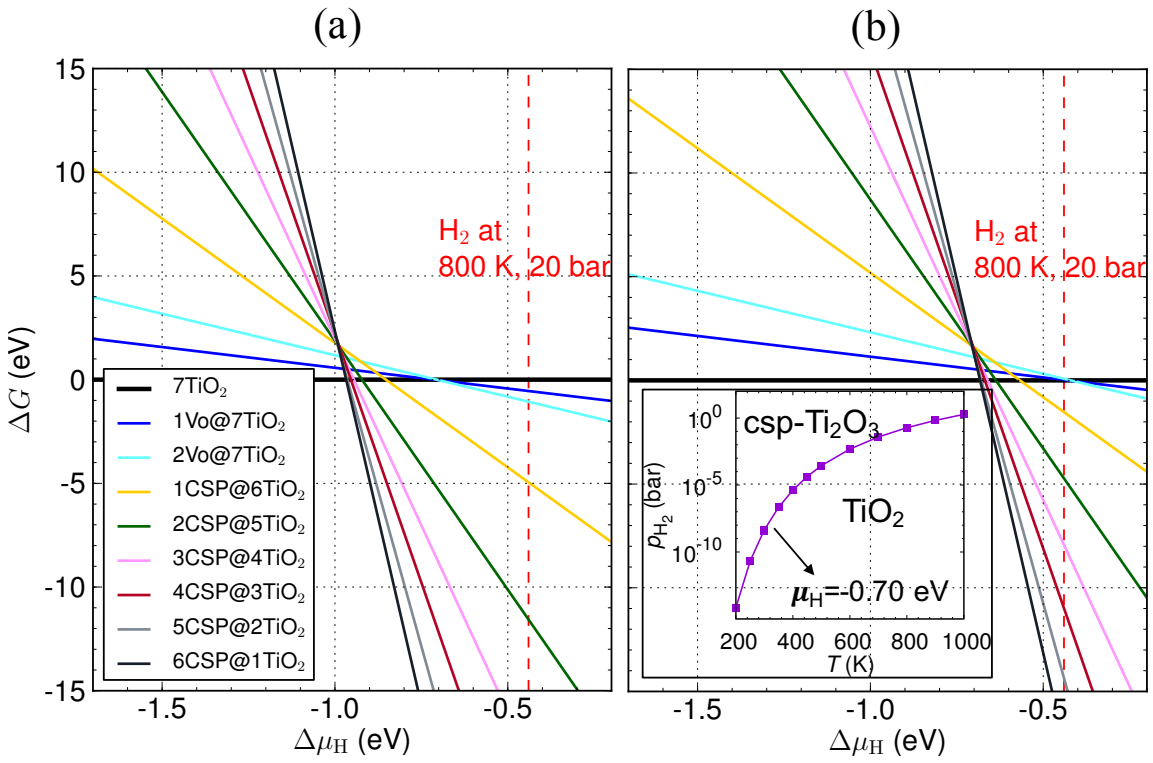

FIG. S8: Formation free energies (ΔG) of the structures listed in Table I in H_2/H_2O atmosphere. ΔG is plotted as a function of the hydrogen (1/2 H_2) chemical potential, with H_2O at (a) T = 800 K and $p_{H2O} = 5\times10^{-8}$ bar and (b) T = 800 K and $p_{H2O} = 10^{-2}$ bar. The reference is a 7-layer slab of pristine anatase TiO_2(101). The inset shows the phase diagram for bulk csp-Ti_2O_3 and TiO_2 as a function of temperature (T) and H_2 pressure.

4 Structural and electronic properties of bulk csp-Ti_2O_3

4.1 csp-Ti_2O_3 and Magneli Ti_3O_5 crystal structure

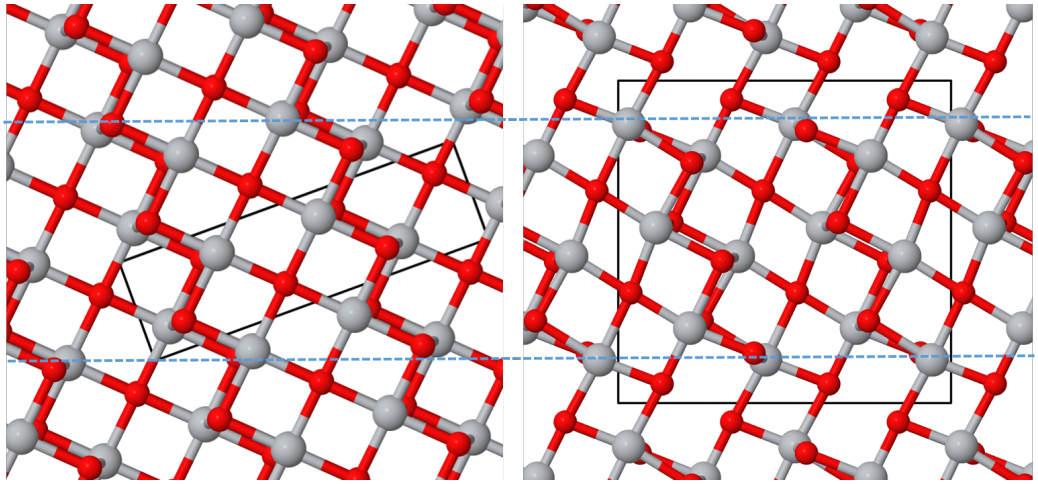

FIG. S9: Crystal structures of csp-Ti_2O_3 and Magneli Ti_3O_5, projected onto the *bc* plane. The black boxes denote the primitive unit cells; within the dashed lines (parallel to (101) plane) the two structures share the same atomic arrangement. With reference to anatase TiO_2, Ti_3O_5 consists of two (101) shear planes for every three layers of TiO_2, that is: $3(2TiO_2) \rightarrow (2TiO_2)+2(Ti_2O_3) = 2Ti_3O_5$, where $3(2TiO_2)$ indicates three layers of TiO_2, each containing two TiO_2 units. In contrast, the csp-Ti_2O_3 structure requires formation of a CSP in every layer of TiO_2, which results in a more compact and symmetric structure.

4.2 Structural parameters

TABLE S3: Optimized lattice parameters of csp-Ti_2O_3, α-Ti_2O_3 and anatase TiO_2, obtained from PBE, PBE+*U* (U=3.0 eV) and HSE06 calculations. Calculations used a variable cell optimization without symmetry constraints. For α-Ti_2O_3 this resulted in a small deviation from perfectly rhombohedral symmetry.

	csp-Ti_2O_3			**α-Ti_2O_3**			**anatase TiO2**		
Parameter	PBE	PBE+U	HSE06	PBE	PBE+U	HSE06	PBE	PBE+U	HSE06
				Lattice constants (Å)					
a	3.984	3.901	3.814	5.516	5.651	5.423	3.797	3.830	3.758
b	2.946	3.165	3.166	5.512	5.578	5.422	3.797	3.830	3.755
c	9.048	9.558	9.616	5.516	5.651	5.421	9.665	9.701	9.631
				Interatomic distances (Å)					
Ti1-Ti2	2.77	2.81	2.72	2.66	2.90	2.64	3.07	3.09	3.06
Ti1-Ti3	2.95	3.16	3.12	4.33	4.20	4.15			
Ti1-Ti4	3.04	3.19	3.14						
Ti1-O1	2.10	2.17	2.15	2.08	2.22	2.08	2.00	2.01	1.98
Ti1-O2	2.02	2.12	2.06	2.08	2.09	2.08	1.94	1.96	1.93
				Angles (degree)					
Ti1-O2-Ti3		96.7	97.7					155.2	154.7
Ti1-O2-Ti2		83.3	82.3		88.1	78.6		102.4	102.6
Ti1-O1-Ti3		96.7	93.1						
Ti3-O1-Ti5		152.4	151.4						
Ti1-O1-Ti2					83.2	78.6			

4.3 Relative energy and magnetization of csp-Ti_2O_3 and α-Ti_2O_3

TABLE S4: Relative total energy and band gap of csp-Ti_2O_3 and α-Ti_2O_3, calculated using PBE+*U* with different *U* values (in eV) and the hybrid HSE06 functional. Reported values were calculated using HSE06 lattice parameters, while values in parenthesis were obtained using lattice parameters optimized with PBE+*U*. For comparison, the computed band gap of anatase TiO_2 is also reported.

Method	$E_{csp\text{-}Ti2O3}$-$E_{\alpha\text{-}Ti2O3}$ (meV/Ti_2O_3)	Band gap (eV)		
		csp-Ti_2O_3	**α-Ti_2O_3**	**TiO_2**
PBE	104 (-60)	metallic	metallic	2.28 (2.17)
PBE+*U* (1.5)	63 (26)	metallic	metallic	2.44 (2.31)
PBE+*U* (1.75)	29 (13)	0.30 (0.35)	0.32 (0.30)	2.47 (2.32)
PBE+*U* (2.5)	-40 (37)	0.91 (0.90)	0.88 (1.00)	2.58 (2.42)
PBE+*U* (3.0)	-63 (61)	1.30 (1.21)	1.24 (1.40)	2.64 (2.48)
PBE+*U* (3.5)	-75 (67)	1.69 (1.80)	1.58 (1.77)	2.71 (2.55)
PBE+*U* (4.0)	-78 (89)	2.06 (2.21)	1.93 (2.24)	2.79 (2.62)
HSE06	-63	1.82	1.90	3.72

TABLE S5 - Computed absolute magnetization (μ_B) per Ti_4O_6 unit cell as a function of U. The total magnetization is always zero. Both α-Ti_2O_3 and csp-Ti_2O_3 are metallic for U ≤ 1.5 eV.

U (eV)	α-Ti_2O_3	csp-Ti2O3
0	0.00	0.00
0.50	0.00	0.00
1.00	0.00	0.91
1.25	0.00	1.41
1.50	1.73	1.98
1.75	2.53	3.07
2.00	3.62	3.34
2.50	3.82	3.66
3.00	3.92	3.83
3.50	4.00	3.92
4.00	4.05	4.00

4.4 Effect of DFT functional on the electronic structure

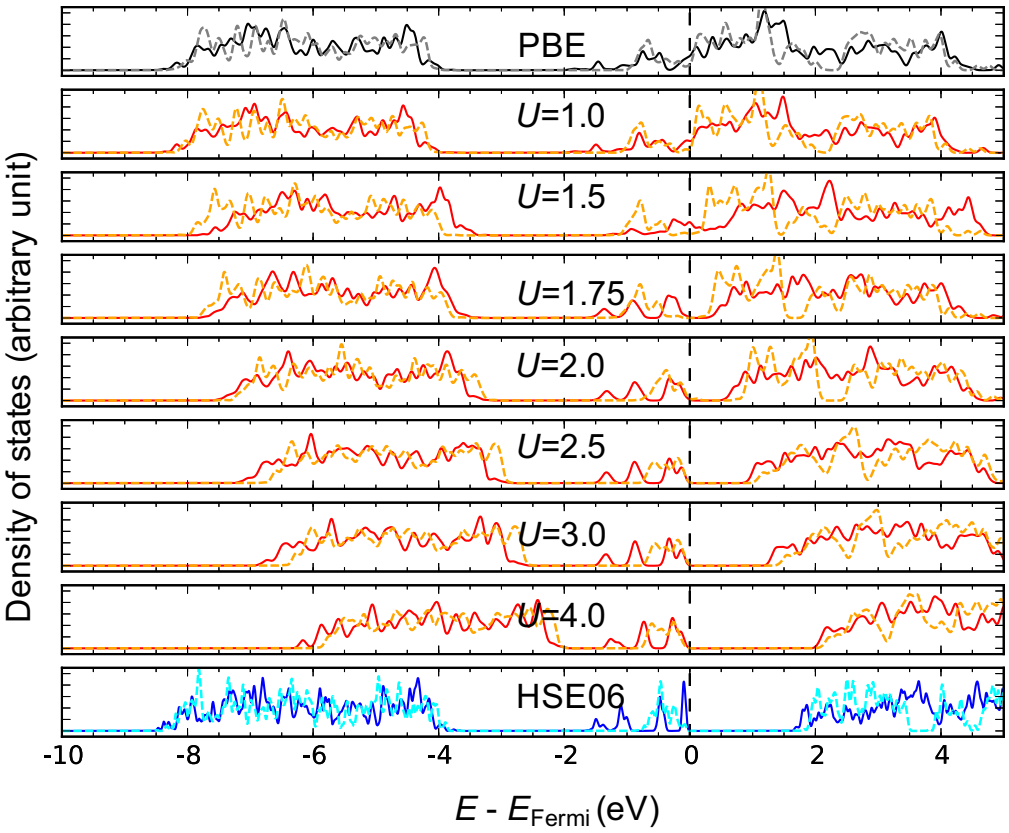

FIG. S10: Density of states of csp-Ti_2O_3 (solid lines) and α-Ti_2O_3 (dashed lines) computed using PBE, PBE+U with different U values in the range 1-4 eV, and the HSE06 hybrid functional. While both csp-Ti_2O_3 and α-Ti_2O_3 are metallic for $U \leq 1.5$ eV, U=1.75 eV gives a band gap of 0.3 eV for α-Ti_2O_3, close to experimental value of 0.1-0.2 eV. The Fermi level is set at the top of the occupied states. Spin up and spin down curves are identical.

4.5 Projected density of states

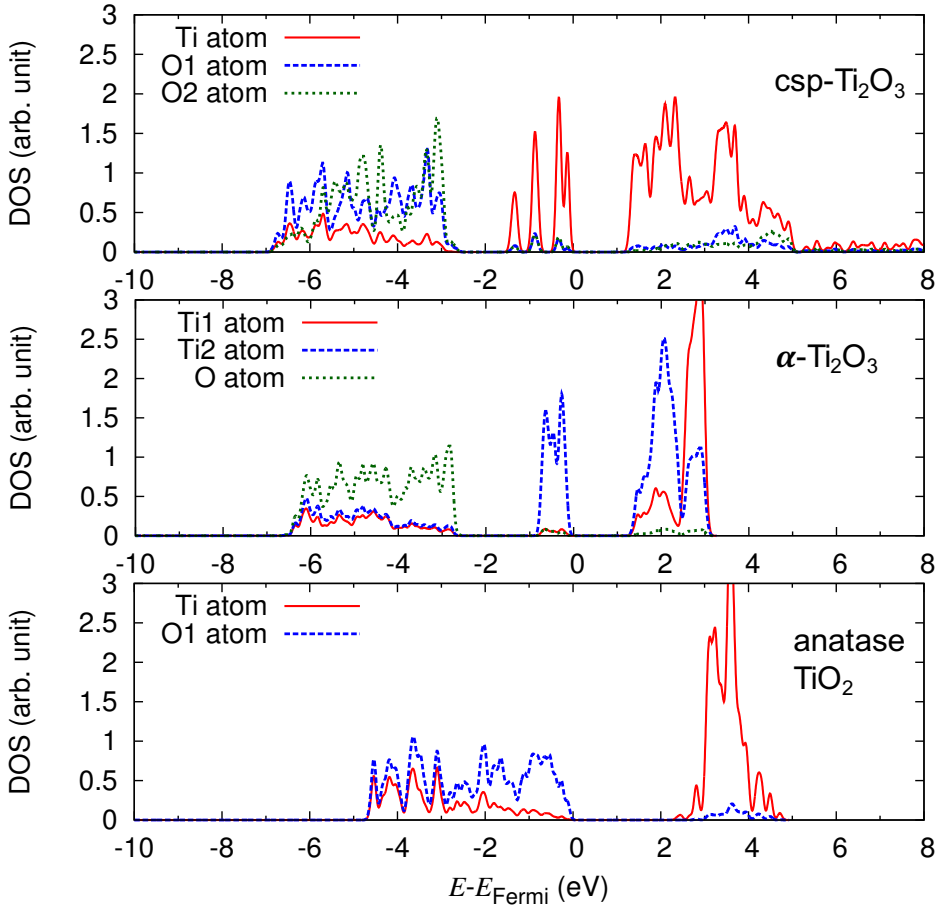

FIG. S11: Partial densities of states of bulk csp-Ti2O3, α-Ti_2O_3 and anatase TiO_2 computed using the PBE+*U* (*U*=3.0 eV) scheme. Inequivalent atoms in the cell are plotted.

* x.zhao@princeton.edu

* aselloni@princeton.edu

[1] P. Giannozzi, S. Baroni, N. Bonini, M. Calandra, R. Car, C. Cavazzoni, D. Ceresoli, G. L. Chiarotti, M. Cococcioni, I. Dabo, A. Dal Corso, S. de Gironcoli, S. Fabris, G. Fratesi, R. Gebauer, U. Gerstmann, C. Gougoussis, A. Kokalj, M. Lazzeri, L. Martin-Samos, N. Marzari, F. Mauri, R. Mazzarello, S. Paolini, A. Pasquarello, L. Paulatto, C. Sbraccia, S. Scandolo, G. Sclauzero, A. P. Seitsonen, A. Smogunov, P. Umari, and R. M. Wentzcovitch, J. Phys. Condens. Matter **21**, 395502 (2009).

[2] B. K. Perdew J. P and M. Ernzerhof, Phys. Rev. Lett. **77**, 3865 (1996).

[3] V. I. Anisimov, J. Zaanen, and O. K. Andersen, Phys. Rev. B **44**, 943 (1991).

[4] Z. Hu and H. Metiu, J. Phys. Chem. C **115**, 5841 (2011).

[5] M. Capdevila-Cortada, Z. Lodziana, and N. López, ACS Catalysis **6**, 8370 (2016).

[6] J. Heyd, G. E. Scuseria, and M. Ernzerhof, J. Chem. Phys. **118**, 8207 (2003).

[7] J. Heyd, G. E. Scuseria, and M. Ernzerhof, J. Chem. Phys. **124**, 14 (2006).

[8] P. Deák, B. Aradi, and T. Frauenheim, Phys. Rev. B **83**, 155207 (2011).

[9] V. Blum, R. Gehrke, F. Hanke, P. Havu, V. Havu, X. Ren, K. Reuter, and M. Scheffler, Comput. Phys. Commun. **180**, 2175 (2009).

[10] D. Vanderbilt, Phys. Rev. B **41**, 7892 (1990).

[11] P. Villars and K. Cenzual, editors , (n.d.) SpringerMaterials database.

[12] S. Lutfalla, V. Shapovalov, and A. T. Bell, J. Chem. Theory Comput. **7**, 2218 (2011).

[13] E. Finazzi, C. Di Valentin, G. Pacchioni, and A. Selloni, J. Chem. Phys. **129**, 154113 (2008).

[14] M. Lazzeri, A. Vittadini, and A. Selloni, Phys. Rev. B - Condens. Matter Mater. Phys. **63**, 1554091 (2001).